1 Combining time-lapse electrical resistivity and self-potential methods to assess soil moisture dynamics in a forested catchment under the rainfall event

4 Wenhang Jiang[1,3], Aimin Liao[1,2], Jiufu Liu[1], Guodong Liu[3]

5 [1]State Key Laboratory of Hydrology-Water Resource and Hydraulic Engineering, Nanjing Hydraulic
6 Research Institute, Nanjing, PR China;
7 [2]Chuzhou Scientific Hydrology Laboratory, Nanjing Hydraulic Research Institute, Chuzhou, PR China;
8 [3]State Key Laboratory of Hydraulics and Mountain River Engineering, Sichuan University, Chengdu,
9 PR China

10 *Correspondence to*: Aimin Liao (seamsun1226@163.com)

11 **Abstract.** Infiltration process and soil moisture dynamics in response to rainfall are crucial for subsurface

12 flow generation, landslide hazard control, and hydro-ecosystem management. Geophysical tools such as

13 the electrical resistivity tomography (ERT) and self-potential (SP) method have proven useful in

14 providing greater temporal and spatial subsurface information and making connections to water content

15 or water flux. In this study, the combination of ERT and SP was used to enhance our understanding of

16 water infiltration processes caused by natural rainfall, subsurface structures, and plant root distribution.

17 We installed 100 ERT electrodes with an electrode spacing of 0.5 m on a tree-covered hillslope to

18 conduct ERT surveys every two weeks from June to October 2022, and increase the frequency of

19 measurements during rainfall events. Non-polarized electrodes were used to measure SP along the

20 hillslope and at various depths. Time-domain reflectometry (TDR) sensors were used to obtain the soil

21 water content as an accurate reference to establish the petrophysical relationship between soil moisture

22 and resistivity. Based on the robustness assessment of these relationships, the results suggest that the

23 Dipole-Dipole configuration may help to obtain a more reasonable interpretation of resistivity at the

24 forest site than the Wenner configuration. The joint interpretation of the SP and ERT results showed that

25 water flow in the study area is dominated by vertical direction, and two preferential flow paths due to the

26 fractured and permeable soil layer interface provide important vertical hydrological connections between

27 deep and shallow soil layers. In addition, the subsurface infiltration processes were strongly influenced

28 by the trees with different root characteristics. Trees with shallow roots tend to retain more water content

29 at the surface. Deep-rooted trees absorb and store water in deeper layers, resulting in significant abrupt

30 changes in the water content of the deeper soil layers. The results of this study provide a basis for

31 investigating the hydrological connectivity and climate sensitivity of soil water distribution by linking

32 rainfall with subsurface information provided by the ERT and SP.

1 Introduction

Precipitation is the most direct and significant source of soil water recharge. Characterizing the effects of precipitation on the infiltration process and soil moisture is critical for the prediction of hydrological pathways (Tetzlaff et al., 2014; Zeng et al., 2016; Hermans et al., 2023), landslide hazard control (Hojat et al., 2019; Nielson et al., 2021; Tsai et al., 2021) and hydro-ecosystem management (Carey et al., 2019). In addition, subsurface structure, vegetation canopies, and highly distributed roots can be the significant contributors to the flow, leading to heterogeneity in soil moisture distribution and associated dynamics (Holbrook et al., 2014; Dick et al., 2018; Vanella et al., 2018). Due to the lack of appropriate tools and the heterogeneity of soil properties in the subsurface, the water dynamics of fluxes and processes and their influences remain poorly understood. Several studies have addressed the dynamics of rainfall infiltration (Cassiani et al., 2009, Travelletti et al., 2012, Carey et al., 2019), moisture variability due to hydraulic redistribution (Robinson et al., 2012; Ain-Lhout et al., 2016; Dick et al., 2018; Guo et al., 2020), soil-root interactions (Garré et al., 2011; Amato et al., 2008; Vanella et al., 2018), and the influence of subsurface structures (Holbrook et al., 2014; Hermans et al., 2023). However, few studies have simultaneously concerned the above multiple influences during the rainfall infiltration process, especially the effects of root characteristics between different tree species on water distribution. This is of great interest in bridging the gap between common modeling approaches and field realities.

Soil moisture dynamics in the subsurface are particularly difficult to characterize. These processes are typically measured using a gravimetric analysis, isotopic tracing, or in situ sensors such as time-domain reflectometry (TDR). These point data or low sampling density prevented a full description of the dynamics of hydrological processes and structures with a high spatial resolution (Zhou et al., 2001; Tetzlaff et al., 2014; Parsekian et al., 2015). Geophysical techniques such as electrical resistivity tomography (ERT) (Srayeddin and Doussan, 2009; Robinson et al., 2012; Beff et al., 2013; Fan et al., 2020; Nielson et al., 2021) and self-potential (SP) (Doussan et al., 2002; Suski et al., 2006; Revil et al., 2012; Voytek et al., 2016, 2019) have been proven to be useful in providing minimally invasive ways to visualize the hydrogeological processes. Cassiani et al. (2009) and Carey et al. (2019) observed the evolution of the wetting peak evolution under transient unsaturated conditions with ERT, when rainfall occurred over a fixed rainfall simulator location (not the entire slope). However, the natural rainfall often

62 occurs over the entire slope, making it difficult to use ERT alone to determine whether the wetting

63 evolution is dominated by lateral subsurface flow or vertical infiltration flow. The SP method has been

64 found to be a complementary methods in characterizing subsurface water flow. Richards et al. (2010)

65 used the ERT and SP and identified nine preferential flow paths in faults. Voytek et al. (2016) identified

66 the hydrologic flowpaths on arctic hillslopes using ERT and SP and provided greater insight into how

67 flow paths and the frost boundary interrelate. However, the combination of the two approaches has rarely

68 been highlighted for investigating the spatial-temporal variation of the subsurface flow in response to

69 rainfall events in the forested site.

70   In the study of soil moisture dynamics using ERT, some used the Dipole-Dipole configuration on

71 account of its improved resolution of vertical variations (Zeng et al., 2016; Greer et al., 2017), while

72 others used the Wenner configuration to account for the horizontal structures (Hojat et al., 2019).

73 Resistivity results are not unique using different measurements or representation, which is a very

74 important source of uncertainty in data interpretation (Giudici, 2000; Clément et al., 2014). Some papers

75 dealt with the depth of investigation (Oldenburg and Li, 1999; Robinson et al., 2012; Carey et al., 2019),

76 and some with the sensitivity (Holbrook et al., 2014) of the resistivity image resulting from different

77 electrode arrays. Ain-Lhout et al. (2016) focused on the ability to recognize resistivity differences in

78 different media, and concluded that the Wenner configuration seems to be the most appropriate as it can

79 differentiate the resistivities of the soil, soil moisture, and argan roots. These studies reported different

80 perspectives to decide electrode arrays for more reliable and representative ERT measurements, and no

81 similar study evaluated the ERT configuration performance by R^2 of the petrophysical relationship

82 between resistivity and water content, especially in the forested site.

83   Here, two-dimensional ERT surveys were coupled with the SP method to characterize the

84 infiltration process in response to rainfall at a resolution of decimeters, at the Nandadish experimental

85 catchment between the Yangtze River and Huai River of eastern China. We also present observations of

86 soil structure and root characteristics at 2 m deepth to assess the impact of structure on water flow

87 processes. Meanwhile, TDR sensors are used to obtain the volumetric water content as an accurate

88 reference to interpret the variation in the electrical resistivity as a function of soil water. The site-specific

89 resistivity and soil water content (SWC, ρ–θ) relationships were developed based on a variety of ERT

90   measuring configurations. This provided a more detailed description of the subsurface hydrologic

91   response through quantitative comparison. And, unlike the single configuration such as Wenner or

92   Dipole-Dipole that is commonly used, we used both configurations and compared them through the R^2

93   of the ρ–θ relationship to obtain the most appropriate measurement configuration for the soil moisture

94   dynamics in response to rainfall at the study site.

95   The objectives of this study were (a) to investigate the potential of a combination of time-lapse ERT

96   and SP for detecting the spatial-temporal variability of soil moisture dynamics in response to the rainfall

97   at the forest field scale. (b) to evaluate the influence of different measuring configuration on the

98   interpretation of resistivity data results, and quantify and visualize subsurface hydrological processes

99   based on the established petrophysical relationship between resistivity and water content, using a spatial

100   ERT and a conventional TDR method. (c) to evaluate the influence of vegetation root systems and

101   subsurface structure on spatial soil moisture patterns and dynamics during the rainfall event by coupling

102   structure and process descriptions. The datasets generated in this paper provide quantitative information

103   on soil moisture dynamics in temporal and spatial dimensions that can improve the understanding of

104   subsurface flow movements during rainfall in the forest field.

105   **2 Methods**

106   **2.1 Study area**

107   The study area, the Nandadish catchment with an area of 7897 m^2, was an experimental catchment

108   belonging to the Chuzhou Scientific Hydrology Laboratory of the Nanjing Hydraulic Research Institute

109   (118°12′37″ E, 32°17′24″ N). The Nandadish catchment is located at a typical climate transition zone

110   (between the Yangtze River and Huai River Basin) from subtropical to the warm temperate of eastern

111   China (Figure 1), with an average annual rainfall (from 1951 to 2016) of 1008 mm. Rainfall is strongly

112   seasonal, with more than 80% of the total rainfall occurring from May to October.

113
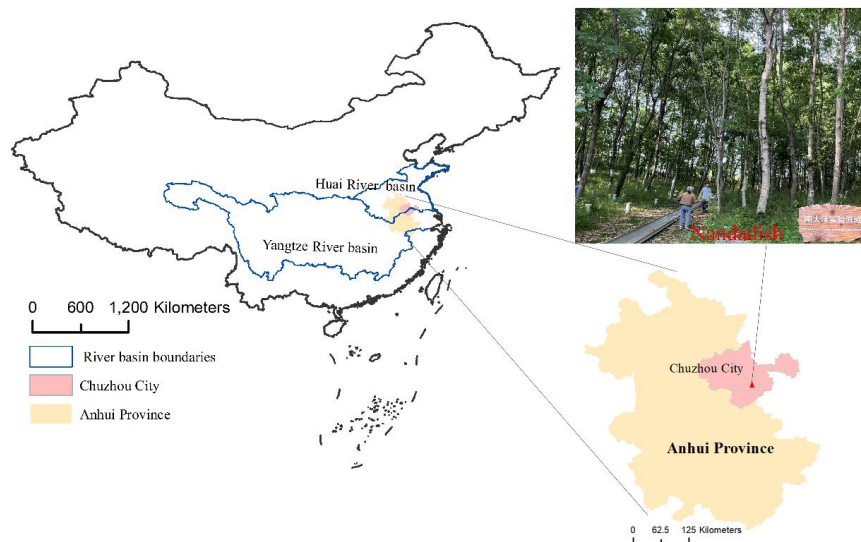
Figure 1: Location of the Nandadish site in the climate transition zone from subtropical to warm temperate, eastern China.

116   The upper part of the Nandadish is forested with a stand density of 1128 trees/ha; the substrate is

117   Mesozoic andesite; the middle part is a loose Quaternary deposit varying from 0.5 to 7.0 m. Its perimeter

118   is separated from the surrounding area by concrete boundary walls and acts as a watershed, making the

119   Nandadish available as a forested critical zone experimental body suitable for hydrological research (Gu

120   et al., 2018). As a typical area of deciduous broadleaved forest, the vegetation in the Nandadish is

121   dominated by Quercus acutissima Carruth. and Broussonetia papyrifera, which account for 67.4% and

122   21.5% of the basal area, respectively.

123   **Table 1: The Nandadish soil texture in the different locations and depths.**

Pits Location	Depth (cm)	Clay % <2 µm	Silt % 2 to 50 µm	Sand % 50 to 2000 µm
	5	11.00	82.74	6.26
	15	11.62	82.95	5.43
	25	11.96	83.02	5.02
Toe	35	12.22	82.74	5.04
	55	13.32	80.87	5.81
	75	12.81	80.45	6.75
	105	14.32	79.65	6.03
Middle	5	13.16	58.64	28.20

	15	9.50	47.27	43.24
	5	12.63	82.31	5.06
	15	11.43	84.01	4.56
	25	12.65	83.07	4.29
Top	35	12.15	83.89	3.97
	55	12.20	83.75	4.06
	75	12.41	83.29	4.30
	105	12.56	83.03	4.41

124   Soil properties analyses were conducted on samples collected from the top, middle, and the toe

125   exploring pits (distributed at 7 m, 25 m and 45 m from the toe of the slope to the top) of a two-dimensional

126   section in the Nandadish (Figure 2), at seven depths of 5, 15, 25, 35, 55, 75, and 105 cm. Three textural

127   fractions, clay (0 to 2 μm), silt (2 to 50 μm), and sand (50 to 2000 μm), were used according to the United

128   States Department of Agriculture (USDA) standards (Cassiani et al., 2015). The soil was uniform in the

129   upper 1.05 m, consisting of a silt loam texture (Table 1), and the mean organic carbon was 10.31 g/kg.

130   The northwest hydrographic slope of the Nandadish crossed a transect of tree roots and open ground

131   (Figure 2). The two-dimensional ERT system, SP electrodes, and the exploring pits were installed on the

132   slope. Three exploring pits were excavated to facilitate the TDR installation and soil sampling The two-

133   dimensional ERT system we installed consists of 100 stainless steel electrodes, 39 cm in length and 1

134   cm in diameter, inserted in the ground at a depth of 15 cm and spaced at a 0.5 m horizontal intervals

135   along the slope (Figure 2). The total length of the surface ERT line was 49.5 m. The relative elevation of

136   each electrode point was measured using a gradiometer and incorporated into the inversion processes.

137   SP measurements in this paper were performed along the section that were nearly parallel to the 2-D

138   ERT section, using Pb-PbCl$_2$ non-polarizing electrodes (developed by China University of Mining and

139   Technology, Wang et al., 2022). The distance between the SP electrodes was 2 m, and the total length of

140   the SP line was 38 m. SP electrodes along the slope were installed out at a depth of approximately 15

141   cm. Meanwhile, we also placed SP electrodes at depths of 5, 15, 25, 35, 55, 75, and 105 cm in the pit

142   position, focusing on monitoring the infiltration processes. On this slope, the obvious surface roots were

143   distributed at 25 to 26 (about 12 m) and 67 to 69 (about 33 m) ERT electrodes from the toe of the slope

144   to the top.
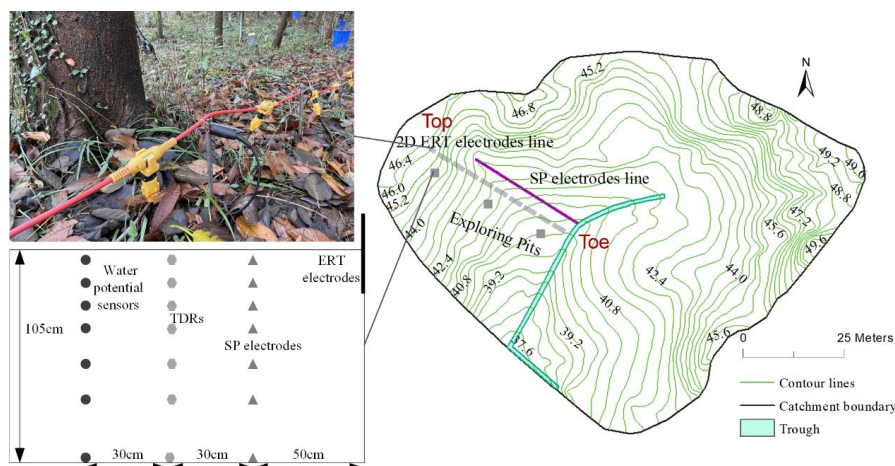
Figure 2: Experimental setup of the slope at the Nandadish site, including the location of ERT electrodes, SP electrodes, TDRs and water potential sensors.

2.2 Electrical resistivity tomography

2.2.1 Data acquisition and processing

The repeated (so called time-lapse) ERT surveys were carried out with the above-mentioned equipment every two weeks from June to October 2022. The measurements were intensified during rainy periods to better represent the rainfall infiltration processes in the subsurface. ERT data were collected using a GD-20 instrument (ST Geomative Co., Ltd, China), which is a multi-channel system for performing ERT, SP and Induced Polarization (IP) measurements. Meanwhile, the GD-20 was equipped with real-time online field monitoring mode to conduct unattended and automated surveys remotely for long periods.

In this work, two different four-pole configurations, Wenner and Dipole-Dipole array, were used for the acquisition of apparent electrical resistivity. Prior each measurement, a contact resistance test between the electrode and the soil was performed to verify the correct operation of the GD-20 monitoring system (Luongo et al., 2012; Zeng et al., 2016). Meanwhile, to avoid anomalies in the resistance measurements during drought caused by poor contact (dry soils can produce a vacuum at the soil-root interface), a little water was added to slightly wet the soil around the electrodes. Each measurement included 1370 measurement points for the Wenner and 1702 points for the Dipole-Dipole, and took approximately 40 minutes and 45 minutes, respectively.

164   While it was not possible to collect reciprocals (current electrodes and potential electrodes are

165 swapped) to determine the fast flow process (Guo et al., 2020), all ERT surveys included only the

166 acquisition data of the direct measurement. After the surveys, all the apparent resistivity data from the

167 ERT measurements were preprocessed to remove noisy data with anomalously high contact resistance

168 (>5000 Ω) (Fan et al., 2020; Vanella et al., 2018).

169   The different soil temperature between deep soil layers of 105 cm and surface soil layers of 5 cm is

170 0 to 15.3°C during the study period. Each pixel of the above filtered apparent electrical resistivity was

171 corrected for the effect of temperature referenced to 18°C using the following relationship (Amato et al.,

172 2008; Srayeddin and Doussan, 2009).

173  $\rho_T = \rho_{T_0}[1 + \lambda(T_0 - T)]$       (1)

174 where ρ_T is electrical resistivity (Ω m) at the temperature T (°C); ρ_{T_0} is electrical resistivity (Ω m) at

175 the temperature T_0 (°C), $T_0 = 18$°C. λ is the temperature correction coefficient, $\lambda = 0.02$.

176 **2.2.2 Data inversion**

177 The true spatial distribution of resistivity can be determined by inversion of the subsurface apparent

178 resistivity within a specified error level and appropriate inversion model constraints (Travelletti et al.,

179 2012; Consoli et al., 2017). To process the time-lapse resistivity data, we used the 2D inversion software

180 EarthImager, developed by Advanced Geosciences Inc., United States. The underdetermined and ill-

181 posed nature of 2D resistivity inverse problems makes the inverse solution inherently nonunique.

182 Additional constraints, or regularization, must be imposed on the model to extract an optimal solution.

183 In this paper, the inversion is performed using a weighted least-squares approach with smoothness

184 constraint (deGroot-Hedlin et al., 1990; Nimmer et al., 2007; AGI 2009). The resistivity distribution is

185 solved by minimizing the objective function as seen below.

186  $\Phi(\mathbf{m}) = [\mathbf{d} - f(\mathbf{m})]^T \mathbf{W}_d [\mathbf{d} - f(\mathbf{m})] + \alpha \mathbf{m}^T \mathbf{R} \mathbf{m}$     (2)

187 where $\mathbf{m}$ is the model vector of resistivities, $\mathbf{m} = \log_e(\boldsymbol{\rho}^{-1})$; $\mathbf{d}$ is the vector of measured resistance data;

188 $f(\mathbf{m})$ is the forward model resistances (the forward operator); T is the matrix transfer; $\mathbf{W}_d$ is an error

189 weighting matrix, i.e., measurement errors, quantified here using a certain percentage of noise as the data

190   weight of 3%. α is a Lagrange multiplier and a stabilizing factor. It determines the amount of model

191   roughness imposed on the model during the inversion. **R** is a roughness operator used to smooth the

192   resistivity distribution and stabilize the inverse solution. The root mean square (RMS) in each survey

193   was calculated to find a resistivity model whose response best fits the measured data (Tsai et al., 2021).

194   An iterative solution is reached when the RMS error in percent is less than 5%.

195   The effect of soil characteristics, such as clay content, on the measured electrical resistivity should

196   be minimized by accounting for differences in resistivity (Srayeddin and Doussan, 2009). To better

197   identify the changes of wetting peaks due to rainfall, we need to select the base (pre-rainfall) resistivity

198   dataset, which can be regarded as an a-priori resistivity model. The time-lapse inversion method was

199   used to invert the difference between the monitor and base datasets. Instead of inverting the monitor

200   dataset alone, the coherent inversion artifacts caused by numerical inaccuracies can be eliminated in the

201   images. The result of the time-lapse inversion is presented as the percent change in resistivity between

202   the two resistivity distribution. The resistivity change was calculated as the relative resistivity difference

203   ($\Delta\rho$, %) (Luongo et al., 2012; Clément et al., 2014) between the monitor (ρ_i, Ω m) and the base data

204   resistivity (ρ_0, Ω m). An increase in resistivity results in a positive percent change and a decrease results

205   in a negative percent change.

206    $$\Delta\rho = \frac{\rho_i - \rho_0}{\rho_0} \times 100 \qquad\qquad (3)$$

207   **2.3 Self potential**

208   SP is a passive geophysical technique that uses a pair of non-polarizing electrodes and a high-impedance

209   voltmeter to detect voltage differences caused by naturally occurring electrical currents. One source of

210   electric current is associated with the flow of water in the subsurface through a permeable or porous

211   material, also called the streaming potential. This current contribution originates from the polar water

212   molecules moving through charged grain surfaces at the fluid-grain interface (Linde et al., 2011; Voytek

213   et al., 2016). Therefore, there is a strong interest to obtain information relative to the fluid flow pattern

214   using a SP method (Sidle et al., 2001; Suski et al., 2006). The depth of investigation for SP is difficult to

215   determine because it depends on the strength of the current source (Voytek et al., 2016). The principle

216 of SP can be described by the Ohm's law and Maxwell's equations as follows (Richards et al., 2010;

217 Linde et al., 2011; Voytek et al., 2019).

218 $j = \sigma E + j_s$ (4)

219 $\nabla \cdot j = 0$ (5)

220 where j is the total current density (Am^{-2}); σE is the conduction current density; σ is the electrical

221 conductivity (Sm^{-1}); E is the electrical field (Vm^{-1}), and $E = -\nabla V$, V is the electrical potential between

222 a reference and a potential electrode from SP method; and j_s is the source current density (Am^{-2}),

223 generated by water movement or other possible current sources. These two equations can help obtained

224 the distribution of V given knowledge of j_s .

225   ERT is sensitive to static or state variables such as water content, while SP is sensitive to dynamic

226 processes such as water flow. For this reason, SP signals can be used to describe the water flow path in

227 hydrology, and measured SP voltages should increase in the direction of flow (Voytek et al., 2019).

228 Rather than one dimensional flow in horizontal (Linde et al., 2011; Voytek et al., 2016) or depth (Doussan

229 et al., 2002), we used SP to evaluate both the two-dimensional soil water movement in this paper. The

230 reference electrode was buried at a depth of approximately 60 cm and located 9 m from the center of the

231 SP section, and the potential difference between the measurement and reference electrodes was recorded

232 with a data collector (DataTaker 85, Biolab, Inc., Australia) at 1 min intervals.

233   Due to telluric currents and induction effects in the cables, many spikes occur in the time series of

234 the SP data. The spikes in the time series were removed while maintaining the total amplitude of the SP

235 variations. The temperature drift of the SP electrodes is very small, 0.01 mV/°C, So the effect of the

236 offset due to temperature can be ignored (Wang et al., 2022).

237 **2.4 Hydrometric and seismic prospecting**

238 Rainfall data were collected from a cluster of tipping bucket rain gauges with the measurement error ≤

239 ±4% located at the automatic weather station 300 m away the Nandadish forest from June to October

240 2022. These rainfall data were collected at 1 minute intervals.

241   The soil water content (SWC) was monitored using a set of TDR probes (TDR315H, Acclima, Inc.,

242 United States). The probes were installed at the toe, middle and top of the slope where the electrical

243 resistivity measuring electrodes were placed, horizontally at seven depths of 5, 15, 25, 35, 55, 75, 105

244   cm in the subsurface. In the middle, as the depth of the bedrock from the ground surface is about 15 cm,

245   only two probes were installed at the depths corresponding to 5 and 15 cm. The soil temperature can also

246   be obtained from the TDR probes, which was required for the temperature correction of the electrical

247   resistivity to a standard temperature. Water potentials were monitored at the same depths as the TDR

248   sensors using Campbell 253 (Campbell 253, Campbell Scientific, Inc., United States). The SWC, soil

249   temperature, and water potentials for each location were collected using a CR1000X data logger at 10

250   min intervals. All sensors were left in place for two weeks to ensure good contact with the surrounding

251   soil.

252   The seismic refraction method was used to create the primary p-wave velocity and obtain the

253   thickness information of weathering layers and the position of the fractured bedrock. The energy from a

254   seismic source travels through the soil in the subsurface and is refracted when it reaches the transition of

255   different material compositions and compaction. The seismic refraction data were recorded between the

256   ERT and SP section using MCSEIS-SX48 (OYO Corporation, Japan) with 24 channel seismographs and

257   28 Hz vertical component geophones spaced at 2.0 m. The last geophone of the previous spread (48 m)

258   became the first geophone of the next spread, this multiple spread allowed 49.5 m spread lengths. The

259   shot was a 5 kg sledgehammer that struck a stainless-steel circular plate with a diameter of 10 cm and a

260   thickness of 4 cm. The first arrival times of the P wave were picked manually on all traces. Based on a

261   2D layered velocity, the inversion was performed until the root-mean-square (RMS) error between the

262   observed and modeled travel times reached 5 %. The inversion results are smooth boundaries with

263   different velocity values. The 0.5 km s^{-1} contour on all final velocity models was used to delineate the

264   transition between loose, highly porous media and the underlying saprolite, and the 1.2 km s^{-1} contour

265   represents the transition between the saprolite and fractured bedrock (Holbrook et al., 2014; Carey et al.,

266   2019).

267   **3 Results**

268   **3.1 Hydrometric observations**

269   Rainfall during the flood season from June to October is shown in Figure 3. The rainfall that occurred on

270   July 4, 2022 and produced a total rainfall of 133.5 mm within 2.6 hours was selected to analyze the

271   infiltration behavior before, during, and after the rainfall event.

272   The changes in typical SWC and water potential of the different vertical soil layers were obtained

273   by averaging of the same layer from pit 1 and pit 3. The SWC remained between 0.18 and 0.45 cm^3cm^{-3},

274   while water potential remained between 0 and -488 kPa during the study period. During the period

275   without rainfall, the soil moisture and water potential measured at different depths decreased steadily.

276   Peaks of the SWC and water potential generally coincided with rainfall events, with the response

277   typically attenuated at deeper soil depths. For example, with the rainfall on August 26, 2022, the SWC

278   and water potential showed an expected increasing tendency in varying degrees only at the near-surface

279   depths of 5, 15, and 25 cm, while there was no significant response at other depths. In addition, the near-

280   surface sensors at 5, 15, and 25 cm depths recorded a lower SWC values than those at the greater depths

281   throughout the flood season, as the top soils dried out due to root water uptake and soil evaporation in

282   forested areas.

283

284
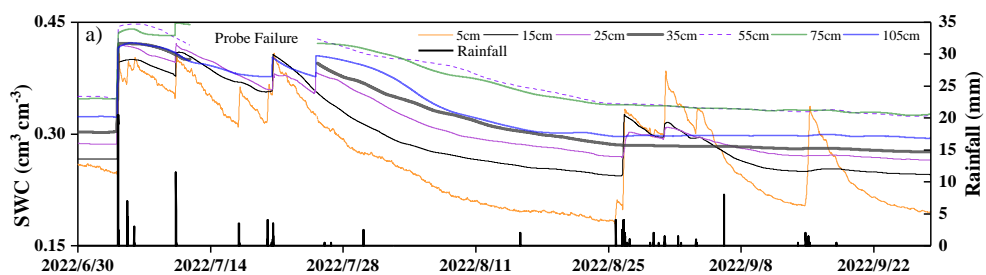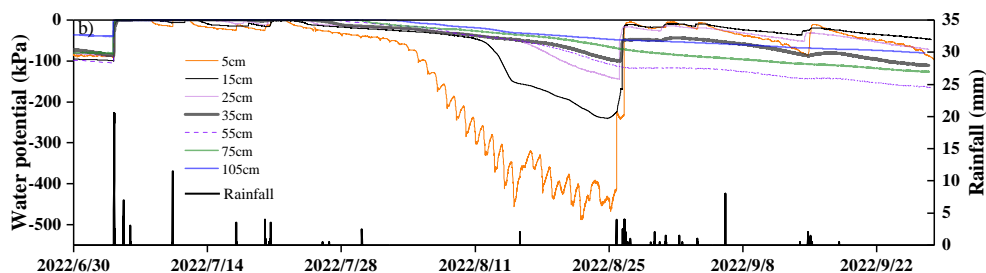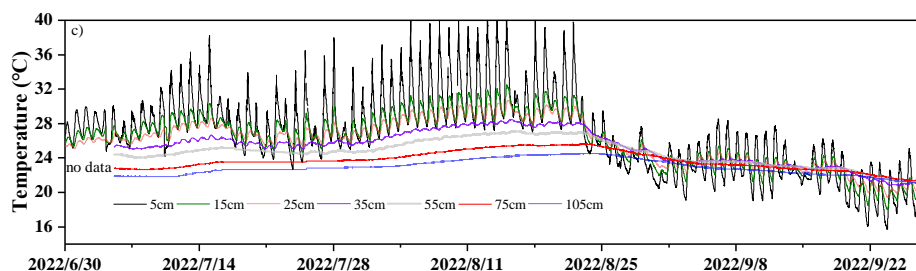
Figure 3: Precipitation, water content, water potential, and soil temperature variation from June to October 2022 at the study site.

During the flood season, the minimum and maximum soil temperatures in the soil layer above 105 cm were 16°C and 42°C, respectively. Soil temperatures showed a significant decrease after the end of August. Spatially, soil temperature varied significantly near the surface, and the amplitude and range of variation decreased with depth. A similarly sinusoidal daily variation of soil temperature was also observed near the surface at 5, 15, 25, and 35 cm, with the highest temperature of the day being reached at around 12:00-14:00.

3.2 Soil Moisture changes response to precipitation

3.2.1 Spatial variation of soil electrical resistivity

The resistivity changes are analyzed for the typical rain event that occurred on July 4, 2022. The mean SWC of 2 days before this rain event in the soil layer above 105 cm was 0.31 cm³cm⁻³. The mean inverted resistivity obtained for each ERT measurement in Figure 4a presents a decreasing trend during rainfall events, from 25.8 to 22.0 Ω m . The resistivity data were corrected based on temperature, so we can reasonably relate this decrease in resistivity to an increase in water content from rainfall infiltration (Travelletti et al., 2012; Greer et al., 2017), assuming no change in the subsurface geologic structure. Four ERT tomograms, shown in Table 2 and Figure 4b, were used to analyze the differential resistivity before, during, and after rainfall. The time-lapse ERT was taken from July 4, 17:35 (35 min after rainfall) to July 5, 08:00 (15 h after rainfall). At 35 min after rainfall (Figure 4b, Tomogram 1), the water content monitored by TDRs in pit 1 and pit 3 was 0.35 and 0.39 cm³cm⁻³, respectively. The lower resistivity at 30 to 49.5 m and the higher resistivity at 0 to 29 m in the subsurface were detected, indicating the initial higher and lower water content, respectively.

308 **Table 2: Summary of ERT inversion before, during, and after rainfall.**

ERT Survey time	No. of Total measurements	No. of rejected measurements	No. of iterations	RMS (%)
Tomogram 1, 35 min after rainfall	1702	71	6	4.71
Tomogram 2, 140 min after rainfall	1689	250	8	4.29
Tomogram 3, 210 min after rainfall	1688	283	8	4.16
Tomogram 4, 15 h after rainfall	1700	205	4	3.48
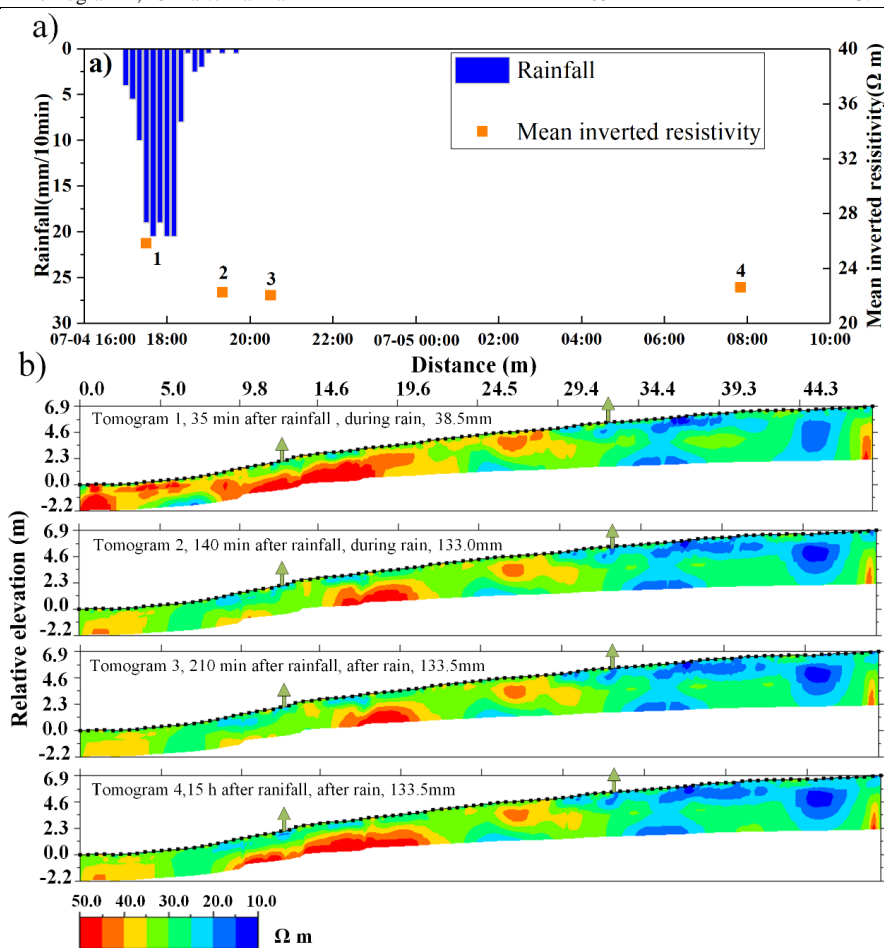
309
310 **Figure 4: ERT monitoring during the rainfall event, with a) Evolution of mean inverted resistivity during**
311 **ERT monitoring versus rain, b) the differenced resistivity model processed before, during, and after rainfall.**

312   Figure 5 shows that 140 minutes after rainfall, a total rainfall of 133.0 mm caused up to a maximum

313 76% decrease in resistivity at 0 to 20 m horizontally, 0 to 2.2 m depth (2.2 m is the depth of investigation,

314 and structures below this depth cannot be used for geological interpretation). Meanwhile, the water

315 content in each soil layer above 105 cm reached more than 0.40 cm^3cm^{-3}, with the average moisture

316 content in pit 1 and pit 3 being 0.42 and 0.43 cm^3cm^{-3}, respectively. The significant decrease in resistivity

317 was concentrated at the toe of the slope rather than the top, which may be attributed to rapid ponding of

318 water caused along the slope. In addition, the site with lower initial water content and its silt loam texture

319 would result in a more pronounced change rate of resistivity change. After 210 minutes, the rain almost

320 stopped and the size of the subsurface accumulation area (blue) no longer increase significantly, but its

321 degree of decreased resistivity and the increase in water content continually increased. At this moment,

322 the average soil moisture in pit 1 and pit 3 were 0.43 and 0.44 cm^3cm^{-3}, respectively, both increased by

323 0.01 cm^3cm^{-3} compared to the water content at 140 minutes after rainfall. As shown in Figure 5, the 10%

324 change in resistivity between Tomograms 2 and 3 indicated that water preferentially reached deeper

325 storage zones through the high permeability zones (blue). Meanwhile, the high permeability zones

326 quickly became high resistivity areas (red) after the 15 hours (the average water content in pit 1 and pit

327 3 were 0.41 and 0.42 cm^3cm^{-3}, respectively). These separate preferential flow paths stimulated by high

328 rainfall intensity, were likely the large voids such as the weathered or fractured rock that could easily

329 move the wet peak during rainfall. Note that the resistivity increases (red or yellow) during precipitation

330 in Figure 5, which is not an unreasonable response to the adding of water in the subsurface. This may be

331 due to the inversion artifacts rather than a true increase in resistivity during the inversion process (Greer

332 et al., 2017).
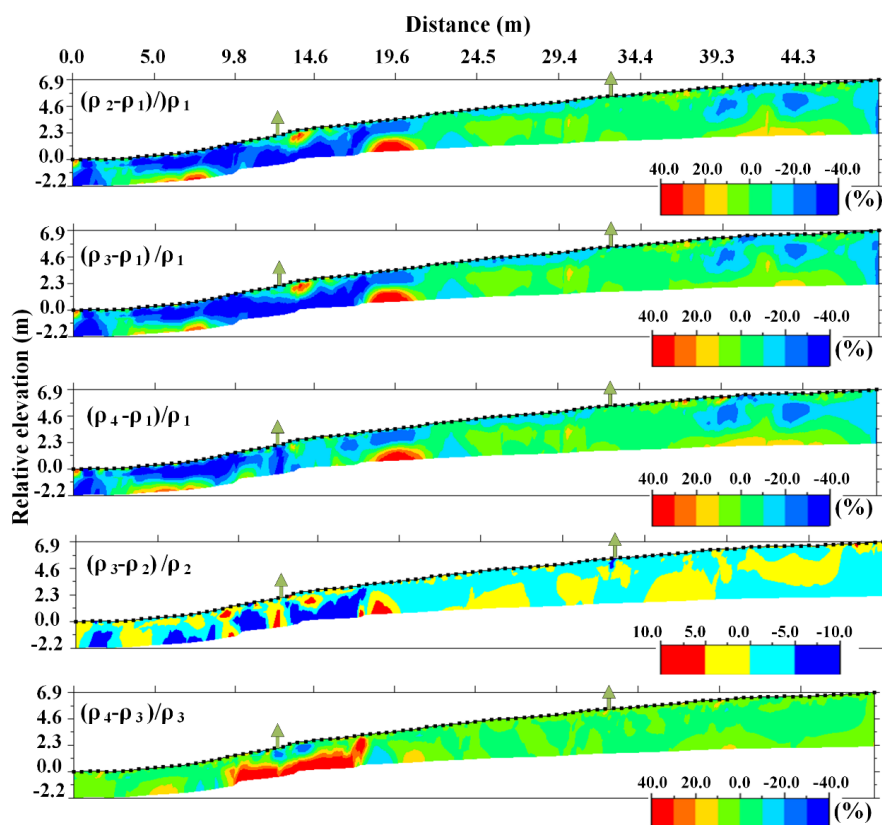
Figure 5: Percentage change in resistivity from different initial model (The first three figures are the percentage changes of resistivity with tomogram 1 as a background, and the next two figures are the percentage changes of resistivity measured at adjacent times).

3.2.2 Quantitative comparison between Soil Moisture and Resistivity

SWC variation is considered to be the most influential parameter for resistivity when the temperature variation is compensated and other factors such as solid constituents remain stable (Clément et al., 2014). Resistivity always links to water content through Archie's law (Archie, 1942; Garré et al., 2011; Tsai et al., 2021) which assumes the clay content is negligible. Whereas in the study area clay content is usually greater than 10%. This condition cannot be considered satisfied. Referring to Travelletti et al. (2012) and (Fan et al., 2015), we directly used a power-law fit in this paper. To map an observed subsurface hydrological response, we developed site-specific resistivity and SWC (ρ–θ) relationships by coupling water content from TDR probes at seven depths with ERT voxels at the corresponding positions. Six ERT surveys using Wenner and Dipole-Dipole respectively, along with TDR measurements, are

347 available for the same position of different pits and probe depths, which are pooled together as soil

348 conditions were similar. Thus, we established relationships for two configurations (Wenner and Dipole-

349 Dipole) during the flood season. As shown in Figure 6, the ρ-θ relationships are negatively correlated to

350 a greater or lesser extent. Note that ρ and θ varied between 18.8 and 49.7 Ω m, and 0.25 and 0.44 cm^{3}cm^{-3},

351 respectively. For the Dipole-Dipole (R^2 = 0.80), the relationship appears much more concentrated than

352 for the Wenner (R^2 = 0.70). A better power fit was obtained using the Dipole-Dipole in this paper.
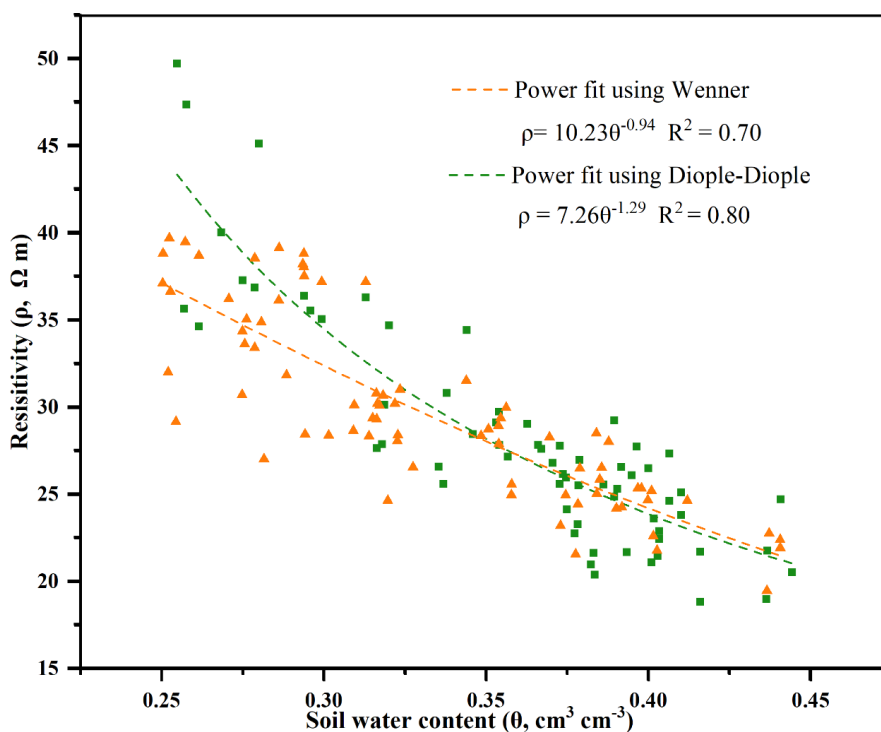
353
354 **Figure 6: The ρ–θ relationship fitted with a power function with Dipole-Dipole or Wenner.**

355 **3.2.3 2D images of soil moisture variation**

356 The spatial variation of soil electrical resistivity cannot be used to directly provide quantitative estimates

357 of the hydrological process. Therefore, based on the site-specific ρ–θ relationship proposed in the study

358 area, 2-D images of SWC variation during the rainfall event were obtained. As shown in Figure 7, high

359 SWC occurred at the top of the hillslope, and decreased rapidly down the slope. There are two preferential

360 flow paths along the soil transect, as indicated by the red arrow. Combined with the seismic wave velocity

361 results, the left preferential flow was connected through the soil-highly fractured bedrock interface,

362 which could be rapidly invaded by water. The right indicated the possible presence of a more permeable

363 saprolite. In addition, the location of the Quercus acutissima Carruth site (the green arrow on the left)

364 became wetter during the rainfall infiltration phase (during rainfall) and the rainfall distribution phase

365 (after rainfall). In contrast, Broussonetia papyrifera site (the green arrow on the right) showed no visible

366 change in wetness. This phenomenon may reflect the regulation of tree species and their root distribution

367 characteristics for the movement of water flow. Unlike Broussonetia papyrifera with its shallow root

368 system, Quercus acutissima Carruth with its deeper roots may take longer to receive the available water

369 flow in the deeper soil layers and have a more pronounced effect on soil moisture changes.
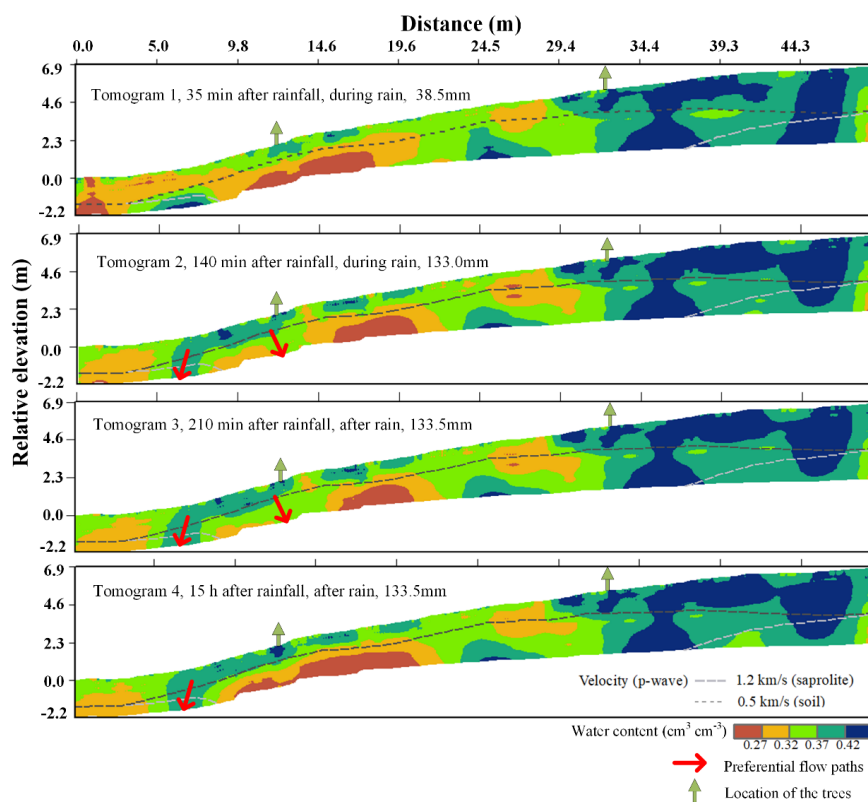
370

371 **Figure 7: 2D images of SWC variation in the soil layer, estimated from the $\rho-\theta$ relationship relationship. The**

372 **green arrow on the left is the location of the Quercus acutissima Carruth and the right is the Broussonetia**

373 **papyrifera.**

3.3 Direction of water movement

Figure 8a shows the SP variability at depths corresponding to the rainfall. The typical rain event on July 4, 2022 resulted in an increase and positive SP signal at different depths. The SP increase at 15, 25, 35 and 55 cm depths occurred at 7, 17, 26, and 32 min after the rainfall. The response of SP near the surface soil layers is more rapid, and the response time is delayed with the increasing depth. In addition, as shown in Table 3, the rainfall caused an increase in the amplitude of the SP signal at a 15 cm depth with 7.5 mV, which is more significant than in the 25 cm soil layers with an increase of 5.0 mV. Meanwhile, the increase in SP amplitude at 35 cm depth was 11.4 mV, which is the maximum increase in SP amplitude at depth. Apparently, the increase in SP amplitude does not always increase with depth.
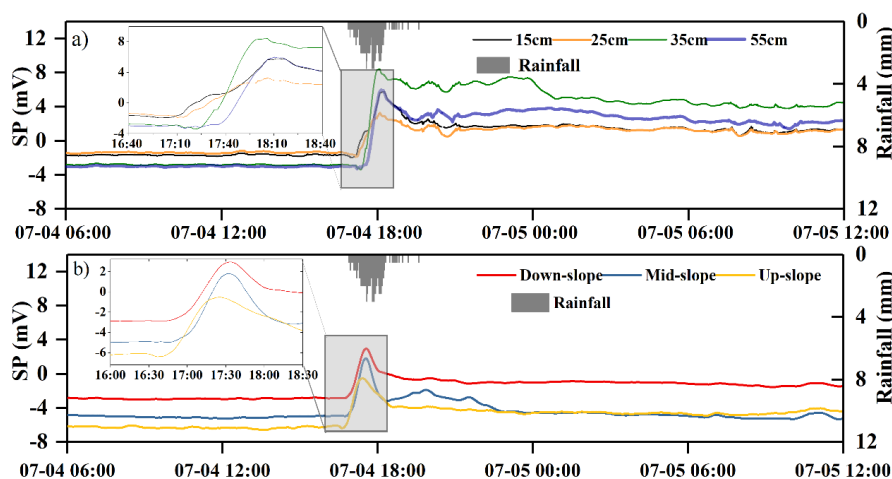
Figure 8: Response of the SP signal to rainfall a) in the vertical depths, and b) in the horizontal direction along the slope.

To depict the lateral water movement, we divided the SP data into up-slope, mid-slope, and down-slope by averaging every six available data except for the first electrode (no data). As shown in Figure 8b and Table 3, the SP signal on the up-slope, mid-slope, and down-slope started to show a response at 3, 3, and 4 min after rainfall, respectively. This faster response time could be attributed to the fact that all SP monitoring electrodes on the slope were installed at a depth of 15 cm, where they are more susceptible to infiltration of rain. The rainfall-induced SP amplitude increase was also high, and the maximum increase reached 7.0 mV. We can also observe the apparent fluctuating variations of SP after the rainfall, which is most likely related to the disturbance of continuous rainfall distribution.

394   **Table 3: Variation of the SP due to the rainfall in the vertical depth and the horizontal position along the**

395   **slope.**

Location	SP electrode depth (cm)	Response time (min)	SP before rainfall (mV)	Max SP during rainfall (mV)	Rainfall-induced SP increase (mV)
Vertical Depths	15	7	-1.7	5.8	7.5
	25	17	-1.7	3.3	5.0
	35	26	-3.0	8.4	11.4
	55	32	-2.9	5.9	8.8
Down-slope	15	4	-2.7	3.2	5.9
Mid-slope	15	3	-4.7	2.3	7.0
Up-slope	15	3	-5.8	-0.6	5.2

396   Since the measured SP voltages should increase in the direction of water flow, this suggests that the

397   water flow down the slope or into deeper soil layers should result in an increase in SP. As shown in Table

398   3, the largest increase of SP in the down-slope location indicates the presence of lateral subsurface flow.

399   However, the magnitude changes between the slope locations are small. The difference between the

400   largest magnitude caused by rainfall in the mid-slope and the up-slope locations is only 1.8 mV (7.0 less

401   5.2). In the vertical depths, the water flows to the 35 cm depth where the SP is maximum. The difference

402   between the maximum SP of 25 cm and 35cm reached 6.4 mV (11.4 less 5.0), which is much larger than

403   the maximum amplitude change of 1.8 mV from the lateral flow on the slope. Therefore, we concluded

404   that the vertical infiltration flow plays a greater role than the lateral flow in the near-surface above 55 cm

405   at the Nandadish site.

406   We proposed a refined conceptual model to represent the water movement in the study area (Figure

407   9). Precipitation rapidly infiltrated into the surface soil layer,and the vertical infiltration was significant

408   in comparison to the lateral transmission flow. The water flow then continues to infiltrate along a more

409   permeable saprolite before entering the fissures in the fractured bedrock. The fractured bedrock layer

410   could be rapidly invaded by water, resulting in preferential infiltration along the lateral or vertical fissures.

411   Once the water encounters the bedrock, a limited lateral flow may occur above the bedrock surface, and

412   some water may infiltrate into the aquifer as deep drainage.
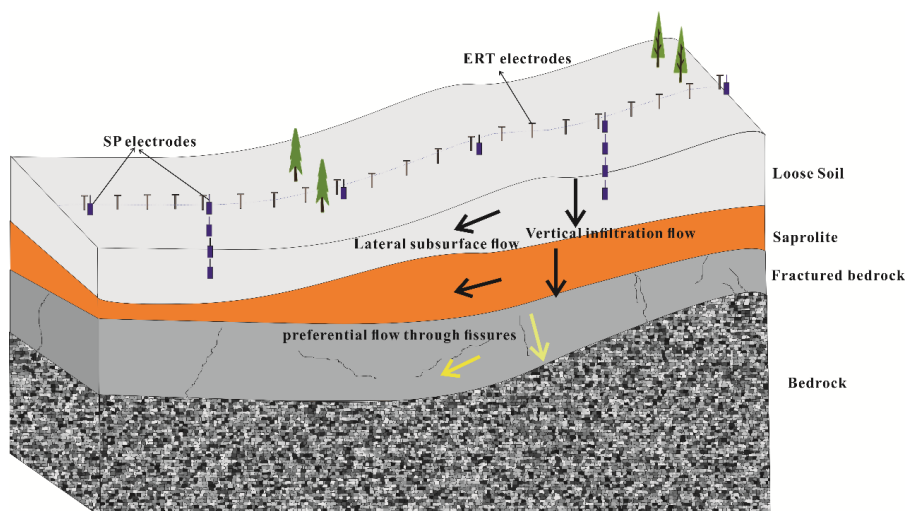
413
414 **Figure 9: The conceptual model to depict the water movement in the Nandadish site.**

415 **4 Discussion**

416 **4.1 Characterizing variation of subsurface flow using time-lapse ERT and SP**

417 The typical heavy rainfall in the study site resulted in a rapid water content response in the shallow soil

418 in a short time, as confirmed by the TDRs (Figure 3). However, the hydrological monitoring could not

419 provide further information to distinguish the infiltration pathways. Here, a combination of time-lapse

420 ERT and SP was presented. ERT allowed us to observe the evolution of the wetting peak under transient

421 unsaturated conditions with a sound spatial resolution, when rainfall occured over a fixed rainfall

422 simulator location (Carey et al., 2019). However, the natural rainfall often occurs over the entire slope,

423 making it difficult to use ERT alone to determine whether the wetting evolution is dominated by lateral

424 subsurface flow or vertical infiltration flow. Therefore, the SP data with a high temporal resolution of 1

425 min interval can be used to explain the evaluation. The two-dimensional (horizontal and depth) SP results

426 in Figure 8 show that the vertical flow rather than the lateral flow dominates, to drainage large amounts

427 of rainwater into the subsoil in the Nandadish forecast catchment. Preferential flow paths are common in

428 forest soils (Sidle et al., 2001; Dick et al., 2018). Two obvious vertical preferential flow paths in Figure

429 7 were observed using ERT, providing important vertical hydrological connections between deep and

430 shallow water during a rainfall event. The development of this combined approach provides the

431 opportunity for upward trends in moisture content and water flow direction, providing a earliest possible

432 warning of runoff and landslide related to rainfall events, which could be extended to other regions.

433  Spatially, the resolution of the shallow (2.2 m) ERT inversion was improved by setting a smaller

434 electrode distance (0.5 m). For temporal resolution, the data collection time with a frequency of 1 to 3

435 hours (a single acquisition takes 45 min) is suitable for monitoring the development of infiltrating water

436 in the unsaturated situation. However, it is necessary to seek improvements in more frequent and faster

437 acquisition equipment that will help improve the temporal resolution in the future research. Besides,

438 mapping subsurface flow at multiple rainfall intensities and types could provide complementary and

439 valuable information to characterize and locate water movements in the Nandadish catchment. This is

440 of great interest for the development of hydrological forecasting models.

441 **4.2 Influence of different ERT configuration on the interpretation of resistivity**

442 The scatter (the larger R^2 of 0.80 in the whole periods) of the ρ–θ relationships using Dipole-Dipole is

443 slightly better than Wenner in Figure 6. The robust agreement between ERT and the SWC from TDR

444 indicates that the usefulness of ERT for the spatial estimation of subsurface flow dynamics in the forest

445 site. Based on this, six additional ERT results measured with the Dipole-Dipole were used to verify the

446 reliability of the proposed ρ–θ relationships in Figure 6 by an evaluating R^2 between the θ from TDR (θ-

447 TDR) and θ from ERT using the ρ–θ relationship (θ-ERT). As presented in Figure 10, the verification

448 results show that the R^2 coefficient was 0.78. These data demonstrate the robustness of the proposed ρ–

449 θ relationship in practical applications, allowing interpretations of ρ in terms of hydrodynamic variations.

450  From a quantitative point of view by using the R^2 as a performance criterion, these results also

451 suggest that in forested areas, the Dipole-Dipole may better help to obtain a more robust resistivity

452 interpretation, when TDR was used to obtain the volumetric water content as an accurate reference. This

453 may be attributed to the fact that the dipole-dipole array has better resolution for vertical structures such

454 as the preferential flow induced by soil cracks (Zeng et al., 2016).
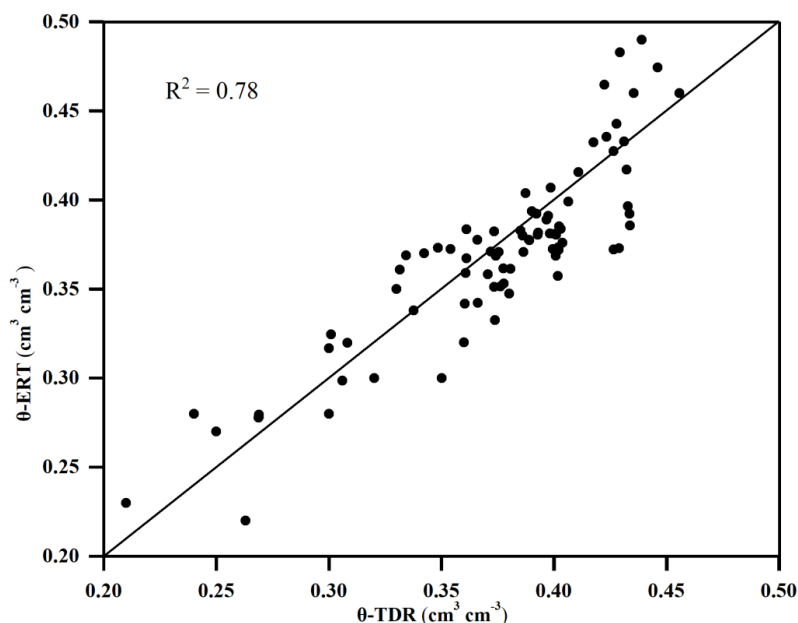
Figure 10: Comparison the SWC from ERT and the SWC from TDR to evaluate the robustness of the eatablished ρ–θ relationship.

4.3 Influence of root characteristics on the water infiltration

The infiltration process and soil moisture dynamics during a rainfall event as confirmed with higher heterogeneity in the resistivity and water content, were linked to the greater subsurface heterogeneity at the Nandadish catchment due to the distributed tree roots and shattered geological structure, both of which are known to be present at the forest site (Cassiani et al., 2015). At the tree root sites, the variation of water content at depth with typical rainfall processes were analyzed by converting the resistivity (Dipole-Dipole measurements) to water content distributions through the quantitative relationship established in this paper. Figure 11 shows an interesting phenomenon that tree species with different root structures can potentially lead to a differential distribution of water. The soil water content before the rainfall at the Quercus acutissima Carruth site was relatively small and drier than that of the Broussonetia papyrifera site, so the degree of change in water content due to rainfall was more pronounced, especially in the shallow surface layer. Generally, the amount of rainfall and the pre-soil condition together determine the degree of change of water content in the subsurface. At the site of Broussonetia papyrifera, the water content decreases with the depth, while at the site of Quercus acutissima Carruth, the trend is

472   exactly the opposite. The difference was more likely caused by the shallow roots of the Broussonetia

473   papyrifera, which tended to retain more soil water at the surface. Instead, Quercus acutissima Carruth is

474   expected to uptake and store water in the deeper depths. At the Quercus acutissima Carruth site, we found

475   a significant and abrupt change in water content at the depth of 1.5 m. This may occur across boundaries

476   of root and soil layers where root activity diverts new rainwater to replace the old and salty water. It is

477   important to notice that deep and shallow root systems may also lead to an additional uncertainty in the

478   estimation of the soil moisture content.

479   In this paper, we have made a two-dimensional explanation using the time-lapse ERT and SP, and

480   found that the substructure and root distribution may directly affect the water content dynamics. Future

481   studies will be directed toward a better understanding of how root characteristics affect the soil water

482   content dynamics, by combining stem-centered 3-D surface and cross-hole ERT measurements with 3-

483   D SP with short acquisition time.
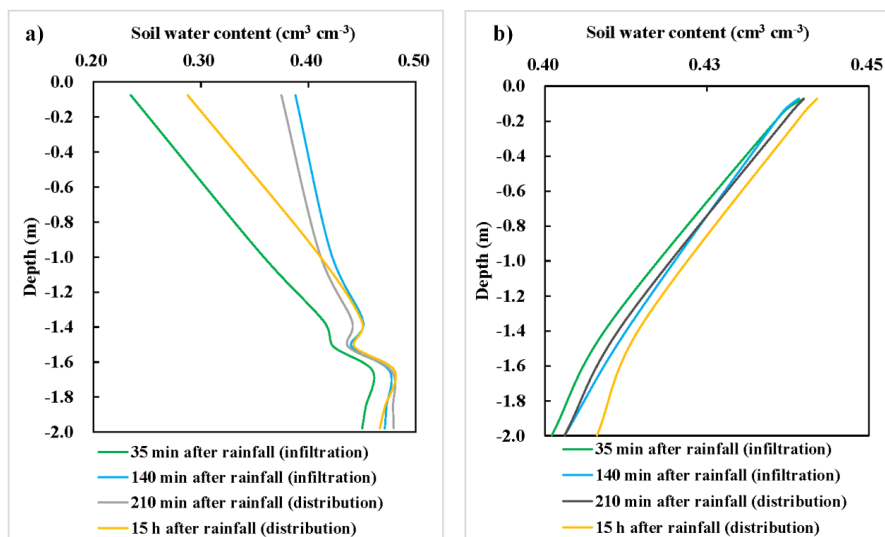
484

485   **Figure 11: Depth profiles with tree locations from electrical resistivity tomography measurements during and**

486   **after rainfall, with a) for the Quercus acutissima Carruth and b) for the Broussonetia papyrifera.**

487   **5 Conclusions**

488   This study contributes a conjunctive utility of time-lapse ERT and SP methods to realize the detailed

489   spatial-temporal measurements of soil moisture dynamics and the water movement direction during

490 precipitation. This helps overcome the limitations of probe- or sample-based methods in terms of sample

491 range or repeatability. Rather than simply describing the water status obtained by ERT, SP can assist in

492 obtaining water flow information that has rarely been emphasized in previous studies. In addition, we

493 developed site-specific ρ–θ relationships based on a variety of ERT measuring configurations and soil

494 moisture conditions. This provided a more detailed description of the subsurface hydrologic response

495 through quantitative comparison. Unlike the single configuration such as Wenner or Dipole-Dipole that

496 is usually used, we used both configurations and compared them by the R^2 of the ρ–θ relationship to

497 obtain the most appropriate measurement configuration. Moreover, information on underground

498 structures obtained from seismic refraction was combined with the water flow processes due to rainfall,

499 to improve the understanding of the fluid movement in the subsurface. Although some artifacts are

500 difficult to resolve, the combined utility of time-lapse ERT and SP methods proved effective in

501 interpreting moisture content development and their direction. The presence of trees with different root

502 characteristics and heterogeneous structures will affect the infiltration and distribution process of rainfall

503 in the soil. Major conclusions are summarized below.

504   (1) It is effective to apply the combination of time-lapse ERT and SP for subsurface flow dynamics

505 during the rainfall. The results provided by the SP clearly showed that the difference between the largest

506 magnitude caused by rainfall along the slope is only 1.8 mV. In the vertical depths, the difference

507 between the maximum SP reached 6.4 mV, which is much larger than the maximum amplitude change

508 of 1.8 mV from the lateral flow on the slope. Therefore, the vertical flow rather than lateral flow

509 dominates, to drain large amounts of rainwater into the subsurface in the Nandadish forecast catchment.

510 Obvious vertical preferential flow paths were observed using ERT, providing important vertical

511 hydrological connections between deep and shallow water during a rainfall event.

512   (2) Based on the established site-specific resistivity and SWC (ρ–θ) relationships by coupling water

513 content from TDR probes at depth with ERT voxels in the corresponding positions, we found that a better

514 power fit was obtained using the Dipole-Dipole with $R^2 = 0.80$ than the Wenner with $R^2 = 0.70$. The

515 Dipole-Dipole configuration may help obtain more robust resistivity interpretations in the forested areas.

516   (3) The infiltration process and soil water moisture dynamics during a rainfall event, as confirmed

517 by higher heterogeneity in the resistivity, were affected by the distributed tree roots and the fractured

518 geological structure. The preferential flow were connected through the soil-highly fractured bedrock

519 interface or permeable saprolite, which could be rapidly invaded by water. Trees with shallow roots

520 tended to retain a greater water content at the surface. Deep-rooted trees absorb and store water in deeper

521 layers, resulting in significant abrupt changes in the water content of the deeper soil layers. The large

522 permeability changes such as preferential flow due to the land cover and characteristics should be

523 incorporated into physical hydrological models, which will be useful for the further refinement of the

524 infiltration mechanism and simulation model development.

525 **Data Availability**

526 Measured raw and inverted time-lapse ERT data are the property of the Chuzhou Scientific Hydrology

527 Laboratory. These data are available from the corresponding author on request.

528 **Authors Contribution**

529 Supervision for this research were acquired by Jiufu Liu and Guodong Liu. The methodology, study

530 conception and experiments were designed and performed by Aimin Liao and Wenhang Jiang. The

531 instrument, software, and data collection were provided by Jiufu Liu and and Aimin Liao. The

532 interpretation of results were handled mainly by Wenhang Jiang. Wenhang Jiang written and prepared

533 the original manuscript with contributions from all co-authors.

534 **Competing Interest**

535 The authors declare that they have no conflict of interest.

536 **Acknowledgements**

537 This study was supported by Nation Nature Science Foundation of China (Grant No. 91847301,

538 92047203), the Science Foundation of Nanjing Hydraulic Research Institute (Y522017), and the Second

539 Tibetan Plateau Scientific Expedition and Research (STEP) program (Grant No. 2019QZKK0203).

References

Advanced Geosciences, Inc. (AGI). Instruction Manual for EarthImager 2D Version 2.4.0 Resistivity and IP Inversion Software. Advanced Geosciences, Inc. Austin, TX, USA.

Ain-Lhout, F., Boutaleb, S., Diaz-Barradas, M. C., Jauregui, J., and Zunzunegui, M.: Monitoring the evolution of soil moisture in root zone system of Argania spinosa using electrical resistivity imaging, Agric. Water Manag., 164, 158–166, https://doi.org/10.1016/j.agwat.2015.08.007, 2016.

Amato, M., Basso, B., Celano, G., Bitella, G., Morelli, G., and Rossi, R.: In situ detection of tree root distribution and biomass by multielectrode resistivity imaging, Tree Physiol., 28, 1441–1448, https://doi.org/10.1093/treephys/28.8.1441, 2008.

Archie, G. E.: The Electrical Resistivity Log as an Aid in Determining Some Reservoir Characteristics, Transactions of the AIME, 146, 54–62, https://doi.org/10.2118/942054-G, 1942.

Beff, L., Günther, T., Vandoorne, B., Couvreur, V., and Javaux, M.: Three-dimensional monitoring of soil water content in a maize field using Electrical Resistivity Tomography, Hydrol. Earth Syst. Sci., 17, 595–609, https://doi.org/10.5194/hess-17-595-2013, 2013.

Carey, A. M., Paige, G. B., Carr, B. J., Holbrook, W. S., and Miller, S. N.: Characterizing hydrological processes in a semiarid rangeland watershed: A hydrogeophysical approach, Hydrol. Process., 33, 759–774, https://doi.org/10.1002/hyp.13361, 2019.

Cassiani, G., Godio, A., Stocco, S., Villa, A., Deiana, R., Frattini, P., and Rossi, M.: Monitoring the hydrologic behaviour of a mountain slope via time-lapse electrical resistivity tomography, Near Surf. Geophys., 7, 475–486, https://doi.org/10.3997/1873-0604.2009013, 2009.

Cassiani, G., Boaga, J., Vanella, D., Perri, M. T., and Consoli, S.: Monitoring and modelling of soil–plant interactions: the joint use of ERT, sap flow and eddy covariance data to characterize the volume of an orange tree root zone, Hydrol. Earth Syst. Sci., 19, 2213–2225, https://doi.org/10.5194/hess-19-2213-2015, 2015.

Clément, R., Moreau, S., Henine, H., Guérin, A., Chaumont, C., and Tournebize, J.: On the value of combining surface and cross-borehole ERT measurements to study artificial tile drainage processes, Near Surf. Geophys., 12, 763–776, https://doi.org/10.3997/1873-0604.2014034, 2014.

567   Consoli, S., Stagno, F., Vanella, D., Boaga, J., Cassiani, G., and Roccuzzo, G.: Partial root-zone drying

568   irrigation in orange orchards: Effects on water use and crop production characteristics, Eur J Agron, 82,

569   190–202, https://doi.org/10.1016/j.eja.2016.11.001, 2017.

570   deGroot-Hedlin, C. and Constable, S.: Occam's inversion to generate smooth, two-dimensional models

571   from magnetotelluric data, Geophysics, 55, 1613–1624, https://doi.org/10.1190/1.1442813, 1990.

572   Dick, J., Tetzlaff, D., Bradford, J., and Soulsby, C.: Using repeat electrical resistivity surveys to assess

573   heterogeneity in soil moisture dynamics under contrasting vegetation types, J. Hydrol., 559, 684–697,

574   https://doi.org/10.1016/j.jhydrol.2018.02.062, 2018.

575   Doussan, C., Jouniaux, L., and Thony, J.-L.: Variations of self-potential and unsaturated water flow with

576   time in sandy loam and clay loam soils, J. Hydrol., 267, 173–185, https://doi.org/10.1016/S0022-

577   1694(02)00148-8, 2002.

578   Fan, B., Liu, X., Zhu, Q., Qin, G., Li, J., Lin, H., and Guo, L.: Exploring the interplay between infiltration

579   dynamics and Critical Zone structures with multiscale geophysical imaging: A review, Geoderma, 374,

580   114431, https://doi.org/10.1016/j.geoderma.2020.114431, 2020.

581   Fan, J., Scheuermann, A., Guyot, A., Baumgartl, T., and Lockington, D. A.: Quantifying spatiotemporal

582   dynamics of root-zone soil water in a mixed forest on subtropical coastal sand dune using surface ERT

583   and spatial TDR, J. Hydrol., 523, 475–488, https://doi.org/10.1016/j.jhydrol.2015.01.064, 2015.

584   Garré, S., Javaux, M., Vanderborght, J., Pagès, L., and Vereecken, H.: Three-Dimensional Electrical

585   Resistivity Tomography to Monitor Root Zone Water Dynamics, Vadose Zone J, 10, 412–424,

586   https://doi.org/10.2136/vzj2010.0079, 2011.

587   Giudici, M.: Fast representation of dipole-dipole geoelectrical data with pseudosections for regional

588   surveys, Annals of Geophysics, 43(2). http://hdl.handle.net/2122/1263

589   Greer, B. M., Burbey, T. J., Zipper, C. E., and Hester, E. T.: Electrical resistivity imaging of hydrologic

590   flow through surface coal mine valley fills with comparison to other landforms, Hydrol. Process., 31,

591   2244–2260, https://doi.org/10.1002/hyp.11180, 2017.

592   Gu, W.-Z., Liu, J.-F., Lin, H., Lin, J., Liu, H.-W., Liao, A.-M., Wang, N., Wang, W.-Z., Ma, T., Yang,

593   N., Li, X.-G., Zhuo, P., and Cai, Z.: Why Hydrological Maze: The Hydropedological Trigger? Review

594   of Experiments at Chuzhou Hydrology Laboratory, Vadose Zone J, 17, 1–27,

595   https://doi.org/10.2136/vzj2017.09.0174, 2018.

596   Guo, L., Mount, G. J., Hudson, S., Lin, H., and Levia, D.: Pairing geophysical techniques improves

597   understanding of the near-surface Critical Zone: Visualization of preferential routing of stemflow along

598   coarse roots, Geoderma, 357, 113953, https://doi.org/10.1016/j.geoderma.2019.113953, 2020.

599   Hermans, T., Goderniaux, P., Jougnot, D., Fleckenstein, J. H., Brunner, P., Nguyen, F., Linde, N.,

600   Huisman, J. A., Bour, O., Lopez Alvis, J., Hoffmann, R., Palacios, A., Cooke, A.-K., Pardo-Álvarez, Á.,

601   Blazevic, L., Pouladi, B., Haruzi, P., Fernandez Visentini, A., Nogueira, G. E. H., Tirado-Conde, J.,

602   Looms, M. C., Kenshilikova, M., Davy, P., and Le Borgne, T.: Advancing measurements and

603   representations of subsurface heterogeneity and dynamic processes: towards 4D hydrogeology, Hydrol.

604   Earth Syst. Sci., 27, 255–287, https://doi.org/10.5194/hess-27-255-2023, 2023.

605   Hojat, A., Arosio, D., Ivanov, V. I., Longoni, L., Papini, M., Scaioni, M., Tresoldi, G., and Zanzi, L.:

606   Geoelectrical characterization and monitoring of slopes on a rainfall-triggered landslide simulator, J Appl

607   Geophy, 170, 103844, https://doi.org/10.1016/j.jappgeo.2019.103844, 2019.

608   Holbrook, W. S., Riebe, C. S., Elwaseif, M., L. Hayes, J., Basler-Reeder, K., L. Harry, D., Malazian, A.,

609   Dosseto, A., C. Hartsough, P., and W. Hopmans, J.: Geophysical constraints on deep weathering and

610   water storage potential in the Southern Sierra Critical Zone Observatory, Earth Surf. Process. Landforms,

611   39, 366–380, https://doi.org/10.1002/esp.3502, 2014.

612   Linde, N., Doetsch, J., Jougnot, D., Genoni, O., Dürst, Y., Minsley, B. J., Vogt, T., Pasquale, N., and

613   Luster, J.: Self-potential investigations of a gravel bar in a restored river corridor, Hydrol. Earth Syst.

614   Sci., 15, 729–742, https://doi.org/10.5194/hess-15-729-2011, 2011.

615   Luongo, R., Perrone, A., Piscitelli, S., and Lapenna, V.: A Prototype System for Time-Lapse Electrical

616   Resistivity Tomographies, International Journal of Geophysics, 2012, 1–12,

617   https://doi.org/10.1155/2012/176895, 2012.

618   Nielson, T., Bradford, J., Pierce, J., and Seyfried, M.: Soil structure and soil moisture dynamics inferred

619   from time-lapse electrical resistivity tomography, Catena, 207, 105553,

620   https://doi.org/10.1016/j.catena.2021.105553, 2021.

621 Nimmer, R. E., Osiensky, J. L., Binley, A. M., Sprenke, K. F., and Williams, B. C.: Electrical resistivity

622 imaging of conductive plume dilution in fractured rock, Hydrogeol J, 15, 877–890,

623 https://doi.org/10.1007/s10040-007-0159-z, 2007.

624 Oldenburg, D. W. and Li, Y.: Estimating depth of investigation in dc resistivity and IP surveys,

625 Geophysics, 64, 403–416, https://doi.org/10.1190/1.1444545, 1999.

626 Parsekian, A. D., Singha, K., Minsley, B. J., Holbrook, W. S., and Slater, L.: Multiscale geophysical

627 imaging of the critical zone: Geophysical Imaging of the Critical Zone, Rev. Geophys., 53, 1–26,

628 https://doi.org/10.1002/2014RG000465, 2015.

629 Revil, A., Karaoulis, M., Johnson, T., and Kemna, A.: Review: Some low-frequency electrical methods

630 for subsurface characterization and monitoring in hydrogeology, Hydrogeol J, 20, 617–658,

631 https://doi.org/10.1007/s10040-011-0819-x, 2012.

632 Richards, K., Revil, A., Jardani, A., Henderson, F., Batzle, M., and Haas, A.: Pattern of shallow ground

633 water flow at Mount Princeton Hot Springs, Colorado, using geoelectrical methods, J. Volcanol.

634 Geotherm. Res., 198, 217–232, https://doi.org/10.1016/j.jvolgeores.2010.09.001, 2010.

635 Robinson, J. L., Slater, L. D., and Schäfer, K. V. R.: Evidence for spatial variability in hydraulic

636 redistribution within an oak–pine forest from resistivity imaging, J. Hydrol., 430–431, 69–79,

637 https://doi.org/10.1016/j.jhydrol.2012.02.002, 2012.

638 Sidle, R. C., Noguchi, S., Tsuboyama, Y., and Laursen, K.: A conceptual model of preferential flow

639 systems in forested hillslopes: evidence of self-organization, Hydrol. Process., 15, 1675–1692,

640 https://doi.org/10.1002/hyp.233, 2001.

641 Srayeddin, I. and Doussan, C.: Estimation of the spatial variability of root water uptake of maize and

642 sorghum at the field scale by electrical resistivity tomography, Plant Soil, 319, 185–207,

643 https://doi.org/10.1007/s11104-008-9860-5, 2009.

644 Suski, B., Revil, A., Titov, K., Konosavsky, P., Voltz, M., Dagès, C., and Huttel, O.: Monitoring of an

645 infiltration experiment using the self-potential method, Water Resour. Res., 42,

646 https://doi.org/10.1029/2005WR004840, 2006.

647   Tetzlaff, D., Birkel, C., Dick, J., Geris, J., and Soulsby, C.: Storage dynamics in hydropedological units

648   control hillslope connectivity, runoff generation, and the evolution of catchment transit time distributions,

649   Water Resour. Res., 50, 969–985, https://doi.org/10.1002/2013WR014147, 2014.

650   Travelletti, J., Sailhac, P., Malet, J.-P., Grandjean, G., and Ponton, J.: Hydrological response of

651   weathered clay-shale slopes: water infiltration monitoring with time-lapse electrical resistivity

652   tomography, Hydrol. Process., 26, 2106–2119, https://doi.org/10.1002/hyp.7983, 2012.

653   Tsai, W.-N., Chen, C.-C., Chiang, C.-W., Chen, P.-Y., Kuo, C.-Y., Wang, K.-L., Lin, M.-L., and Chen,

654   R.-F.: Electrical Resistivity Tomography (ERT) Monitoring for Landslides: Case Study in the Lantai

655   Area, Yilan Taiping Mountain, Northeast Taiwan, Front. Earth Sci., 9, 737271,

656   https://doi.org/10.3389/feart.2021.737271, 2021.

657   Vanella, D., Cassiani, G., Busato, L., Boaga, J., Barbagallo, S., Binley, A., and Consoli, S.: Use of small

658   scale electrical resistivity tomography to identify soil-root interactions during deficit irrigation, J. Hydrol.,

659   556, 310–324, https://doi.org/10.1016/j.jhydrol.2017.11.025, 2018.

660   Voytek, E. B., Rushlow, C. R., Godsey, S. E., and Singha, K.: Identifying hydrologic flowpaths on arctic

661   hillslopes using electrical resistivity and self potential, Geophysics, 81, WA225–WA232,

662   https://doi.org/10.1190/geo2015-0172.1, 2016.

663   Voytek, E. B., Barnard, H. R., Jougnot, D., and Singha, K.: Transpiration- and precipitation-induced

664   subsurface water flow observed using the self-potential method, Hydrol. Process., hyp.13453,

665   https://doi.org/10.1002/hyp.13453, 2019.

666   Wang, H., Fu, S.J., Ge, S.Y., Ma, F.Y., Song, B.Y., and Luo, J.C..: Development and performance testing

667   of maintenance free ultra-low noise solid unpolarized electrodes. Geophysical and Geochemical

668   Exploration, 46 (3): 714-721, https://doi.org/10.11720/wtyht. 2022.1386, 2022.

669   Zeng, R. Q., Meng, X. M., Zhang, F. Y., Wang, S. Y., Cui, Z. J., Zhang, M. S., Zhang, Y., and Chen, G.:

670   Characterizing hydrological processes on loess slopes using electrical resistivity tomography – A case

671   study of the Heifangtai Terrace, Northwest China, J. Hydrol., 541, 742–753,

672   https://doi.org/10.1016/j.jhydrol.2016.07.033, 2016.

673   Zhou, Q. Y., Shimada, J., and Sato, A.: Three-dimensional spatial and temporal monitoring of soil water

674   content using electrical resistivity tomography, Water Resour. Res., 37, 273–285,

675   https://doi.org/10.1029/2000WR900284, 2001.

676